RESEARCH ARTICLE
SPACE PHYSICS: MAGNETOSPHERIC PHYSICS

Earth and Planetary Physics
8: 1–8, 2024
doi: 10.26464/epp2023058

Simulation of the SMILE Soft X-ray Imager response to a southward interplanetary magnetic field turning

Andrey Samsonov[1]*, Graziella Branduardi-Raymont[1], Steven Sembay[2], Andrew Read[2], David Sibeck[3], and Lutz Rastaetter[3]

[1]Mullard Space Science Laboratory, University College London, Dorking RH5 6NT, UK;

[2]Leicester University, Leicester LE1 7RH, UK;

[3]Goddard Space Flight Center, National Aeronautics and Space Administration, Greenbelt, MD 20771, USA

Key Points:

- We simulate Solar wind Magnetosphere Ionosphere Link Explorer (SMILE) Soft X-ray Imager (SXI) count maps for an event with a southward interplanetary magnetic field turning.
- We find the magnetopause standoff distance from the SXI count maps by using assumptions about the magnetopause shape.
- The maximal difference between the estimated standoff distance from the count maps and the one obtained from the magnetohydrodynamic (MHD) solution is 0.24 R_E.

Citation: Samsonov, A., Branduardi-Raymont, G., Sembay, S., Read, A., Sibeck, D., and Rastaetter, L. (2024). Simulation of the SMILE Soft X-ray Imager response to a southward interplanetary magnetic field turning. *Earth Planet. Phys.*, *8*(1), 1–8. http://doi.org/10.26464/epp2023058

Abstract: The Solar wind Magnetosphere Ionosphere Link Explorer (SMILE) Soft X-ray Imager (SXI) will shine a spotlight on magnetopause dynamics during magnetic reconnection. We simulate an event with a southward interplanetary magnetic field turning and produce SXI count maps with a 5-minute integration time. By making assumptions about the magnetopause shape, we find the magnetopause standoff distance from the count maps and compare it with the one obtained directly from the magnetohydrodynamic (MHD) simulation. The root mean square deviations between the reconstructed and MHD standoff distances do not exceed 0.2 R_E (Earth radius) and the maximal difference equals 0.24 R_E during the 25-minute interval around the southward turning.

Keywords: magnetopause; magnetic reconnection; solar wind charge exchange; southward interplanetary magnetic field; numerical modeling; Solar wind Magnetosphere Ionosphere Link Explorer (SMILE); Soft X-ray Imager

1. Introduction

The Solar wind Magnetosphere Ionosphere Link Explorer, or SMILE, is a joint mission between the European Space Agency and the Chinese Academy of Sciences that is due for launch in 2025. The SMILE mission will study the dynamic response of the terrestrial magnetosphere to solar wind variations in a revolutionary new way, by using the Soft X-ray Imager (SXI). Soft X-rays are emitted in the magnetosheath and cusps when heavy solar wind ions (e.g., O^{7+}) interact with exospheric neutrals (hydrogen) via solar wind charge exchange (SWCX; e.g., see Cravens et al., 2001; Robertson and Cravens, 2003; Carter et al., 2010; Kuntz et al., 2015). The heavy ion picks up an electron from the neutral. This electron first enters into a high-energy orbit, but then moves to a lower energy orbit emitting a photon. Using a successive set of soft X-ray images of the dayside magnetosheath and magnetosphere, the SXI collects information about the magnetopause motion in response to solar wind variations. Finding a three-dimensional magnetopause shape from two-dimensional X-ray images is not a trivial task; therefore, several methods have recently been developed and applied for different solar wind conditions (Collier and Connor, 2018; Jorgensen et al., 2019a, b, 2022; Sun TR et al., 2019, 2020; Guo YH et al., 2022; Samsonov et al., 2022a, b; see also review by Wang C and Sun TR, 2022). These methods assume either that the shape of the magnetopause can be expressed by Shue's (Shue JH et al., 1997) modified model (Jorgensen et al., 2019a) or that the magnetopause does not move as the spacecraft follows a certain path along its orbit (Collier and Connor, 2018). A common assumption is that the maximum of the integrated X-ray emissivity occurs along the line-of-sight tangent to the surface of the magnetopause (Sibeck et al., 2018). Samsonov et al. (2022b) verified this assumption and concluded that the maximum of the integrated emissivity occurs at the outer edge of a wide magnetopause layer produced by the magnetohydrodynamic (MHD) simulations (see also Read, 2024, this issue).

The SMILE mission will study the manner in which energy and plasma enter the magnetosphere. The main mechanism for energy transport through the dayside magnetopause is magnetic reconnection. SMILE will explore the phenomenon of magne-

Correspondence to: A. Samsonov, a.samsonov@ucl.ac.uk
Received 18 MAR 2023; Accepted 04 JUL 2023.
First Published online 31 JUL 2023.

topause reconnection and will seek to determine when and where transient and steady reconnection states dominate (Branduardi-Raymont et al., 2018). The southward orientation of the interplanetary magnetic field (IMF) is a favorable condition for dayside magnetopause reconnection. In this study, we look for events with a southward IMF turning (ST) in which the IMF orientation changes rapidly from northward to southward. Usually, the magnetosphere and magnetopause location remain relatively quiet for a northward IMF (known as a "closed magnetosphere"). If the IMF then rotates southward, dayside magnetopause reconnection begins. One of the reconnection signatures is the earthward magnetopause motion, also known as magnetopause erosion, in which the magnetic flux reconnected from the dayside magnetosphere is transferred to the magnetotail (Aubry et al., 1970; Maltsev and Lyatsky, 1975; Tsyganenko and Sibeck, 1994). By observing the large-scale magnetopause response to an ST event, we will better understand the nature of the reconnection process.

Reconnection is not the only reason for global-scale magnetopause motion. The magnetopause response to solar wind dynamic pressure variations is, overall, even stronger than the response to changes in the IMF B_z (we use Geocentric Solar Magnetospheric (GSM) coordinates throughout the paper). In the event simulated in this work, we compare the changes in the magnetopause standoff distance in response to an increase in the dynamic pressure and an ST. Connor et al. (2021) have recently simulated two artificial cases, with an ST and a sudden enhancement of the solar wind dynamic pressure. The authors compare the soft X-ray and energetic neutral atom images, which can be obtained by a virtual spacecraft from two positions in the terminator plane.

In this study, we use the global MHD model to calculate the X-ray emissivity in the magnetosheath and cusps and the *sxi_sim* code (Sembay et al., 2024 this issue) to calculate the integrated emissivity and SXI count maps. The *sxi_sim* code reproduces the expected output of the SXI instrument for a given three-dimensional emissivity cube; therefore, we can check that we will be able to resolve the expected earthward magnetopause motion in a real case with the ST. All details concerning the simulation of the integrated emissivity and count maps have been presented by Samsonov et al. (2022a, b). We choose a case in which the IMF B_z changes from a large positive value to a large negative value. This article is organized as follows. The next section contains a brief description of the MHD model and the *sxi_sim* code and presents the solar wind conditions. In the third section, we show the results of the simulations. The last section provides conclusions.

2. Numerical Models and Solar Wind Conditions

We use the Space Weather Modeling Framework (SWMF) global MHD model (Tóth et al., 2005, 2012) version 20180525 available through the Runs-on-Request from the Community Coordinated Modeling Center at the Goddard Space Flight Center. The SWMF model uses an adaptive structured Cartesian grid. In this study, we use a run with the best spatial resolution of 0.125 R_E (Earth radius) in the whole dayside magnetosphere, magnetosheath, and cusps. Figure 1 shows the solar wind OMNI data used by the numerical model for its upstream boundary condition. The magnetic field component B_x is set to zero to keep the $\nabla\cdot\boldsymbol{B}=0$ constraint (Powell et al., 1999). We simulate the 3-hour interval from 09:00 to 12:00 universal time (UT) on March12, 2012. A discontinuity with an ST occurs at 10:41 UT. This discontinuity is preceded by one hour of a strong northward IMF and followed by more than one hour of a strong southward IMF (until the end of the considered time interval). The density, of approximately 40 cm^{-3}, stays high during the event. The velocity, of nearly 500 km/s (occasionally slightly more), is also larger than average. The density and velocity increase at 09:26 UT at the beginning of the time interval, which results in significant magnetospheric compression. However, the solar wind dynamic pressure remains nearly constant through the ST discontinuity.

The soft X-ray emissivity P_X is calculated by the following expression:

$$P_x = \alpha N_{SW} N_H V_{rel},$$

where $\alpha = 10^{-15}$ eV cm^2, N_{SW} is the solar wind and magnetosheath density, N_H is the exospheric neutral hydrogen density, and V_{rel} is the relative velocity calculated as a square root of the velocity and thermal velocity squares. We obtain N_{SW} and V_{rel} from the MHD simulations. We assume that the exospheric neutral density N_H falls off with R^{-3}, where R is the geocentric distance (Cravens et al., 2001). We calculate P_X in a three-dimensional cube and use it for calculations of the integrated line-of-sight I_X emissivity and SXI count maps.

The SXI count map is derived by using the instrument simulator software *sxi_sim* developed by the SXI instrument team (see Sembay et al., 2024 this issue). The maps are the expected counts from the foreground SWCX emission within the SXI field of view (FOV) in user-defined pixels and for a given user-defined integration time. The simulator calculates the expected foreground (SWCX) and background (typical X-ray astrophysical background plus particle-induced background) input components, passes the photon components through the full instrument response, and then combines them to derive an estimate of the total counts within the FOV. Poisson noise is then added to the total counts, and the background components are subtracted to leave an estimate of the foreground emission with the appropriate level of noise. To produce the SXI count map, we take into account a reduction in image brightness at the edges of the FOV (i.e., the instrument vignetting function).

The spacecraft location and the SXI FOV change with time. But because we will mainly focus on a relatively short time interval near the ST (25 minutes), we will fix the spacecraft location near its apogee at (6.57, −5.94, 17.33) R_E and the SXI aim point (the center of the FOV) at (7.0, 0.0, 0.0) R_E. The aim point has been chosen to be close to the magnetopause subsolar point when the ST interacts with the magnetosphere.

3. Results

3.1 Standoff Distance in MHD Simulations

Figure 2 shows the magnetopause standoff distance obtained from the MHD simulation. More precisely, it shows the location of the boundary between open and closed magnetic field lines at the subsolar point (closed magnetic field lines are connected to the Earth by both ends). The vertical lines indicate times when the

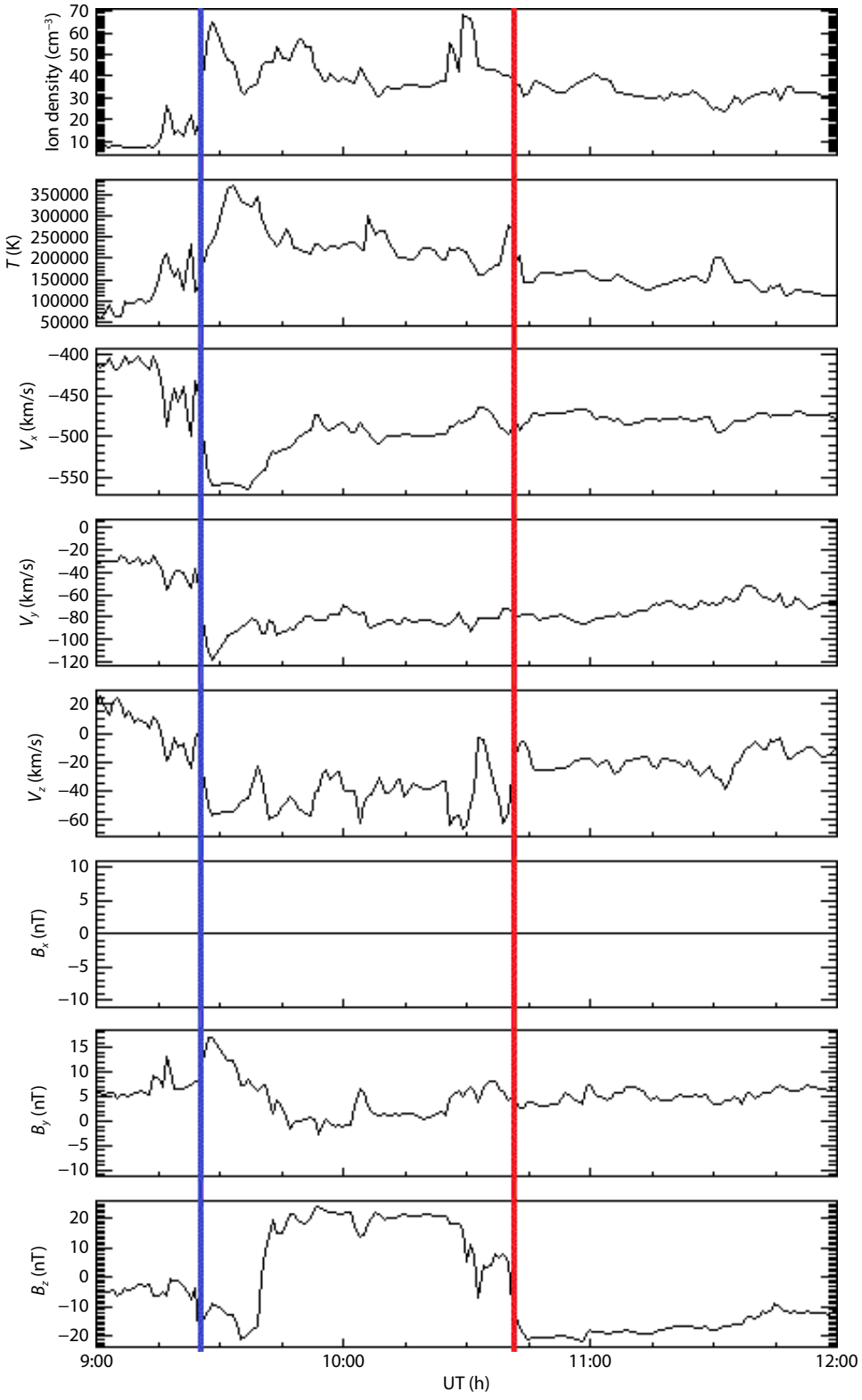

Figure 1. The solar wind conditions on 09:00–12:00 UT March 12, 2012, used for the MHD simulation. The vertical blue and red lines mark the discontinuities with the increase in the solar wind dynamic pressure and the southward turning respectively.

magnetopause moves toward the Earth in response to the jump of the solar wind dynamic pressure (blue line) and in response to the ST (red line). The first response is faster and stronger than the second. The standoff distance decreases by approximately 2 R_E at 09:30 UT and by approximately 1 R_E between 10:50 and 11:07 UT. We compare these two responses to point out that the dynamic pressure makes a stronger impact on the standoff distance than the IMF B_z even if the changes in B_z are significant. We also draw the three horizontal lines to indicate the region where we can observe the maximum of the integrated emissivity by using given

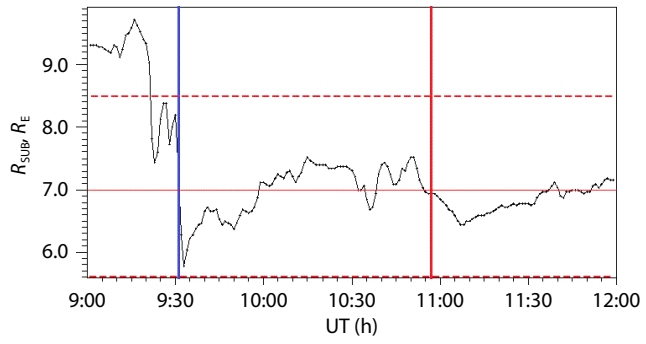

Figure 2. The magnetopause standoff distance obtained in the MHD simulations. The vertical blue and red lines indicate the earthward magnetopause motion in response to an increase in the dynamic pressure and the southward turning. The red horizontal lines mark the region around $x = 7\ R_E$ in which the maximum of emissivity can be detected (see details in the text).

assumptions about the spacecraft location and the SXI aim point. The SXI FOV is 16° × 27°, which gives us an interval of ±8° in the horizontal direction (along the Sun–Earth line), but we exclude the edges of the SXI FOV (~3°) where we cannot confidently determine the location of the emissivity maximum. Therefore, we measure the angle of 5° on both sides around the aim point at $x = 7\ R_E$ (solid red line). This results in the interval from 5.5 to 8.5 R_E (dashed red lines) along the Sun–Earth line where we can observe the emissivity maximum for the fixed aim point and spacecraft location. Accordingly, the magnetopause position cannot be observed until 09:20 UT because the subsolar point is located out of the FOV. We should note here that the assumption about the stationarity of the spacecraft position and FOV is not valid for a 3-hour interval; moreover, the expected SXI FOV may differ from the one that we use in this study.

3.2 Integrated Emissivity and SXI Count Maps

Using the *sxi_sim* code, we integrate the emissivity and calculate count maps every five minutes beginning from 10:50 UT. Figure 3 shows the results obtained. The Earth is to the left side, and the Sun is to the right side. The SXI instrument is oriented in such a way that the SXI aim point is directed toward the approximate subsolar magnetopause, at (7.0, 0.0, 0.0) R_E. The $\phi = 0$ in Figure 3 corresponds to the plane passing through the spacecraft and the Sun–Earth line. The $\theta = 0$ plane is orthogonal to the $\phi = 0$ plane and contains the location of the spacecraft and the aim point.

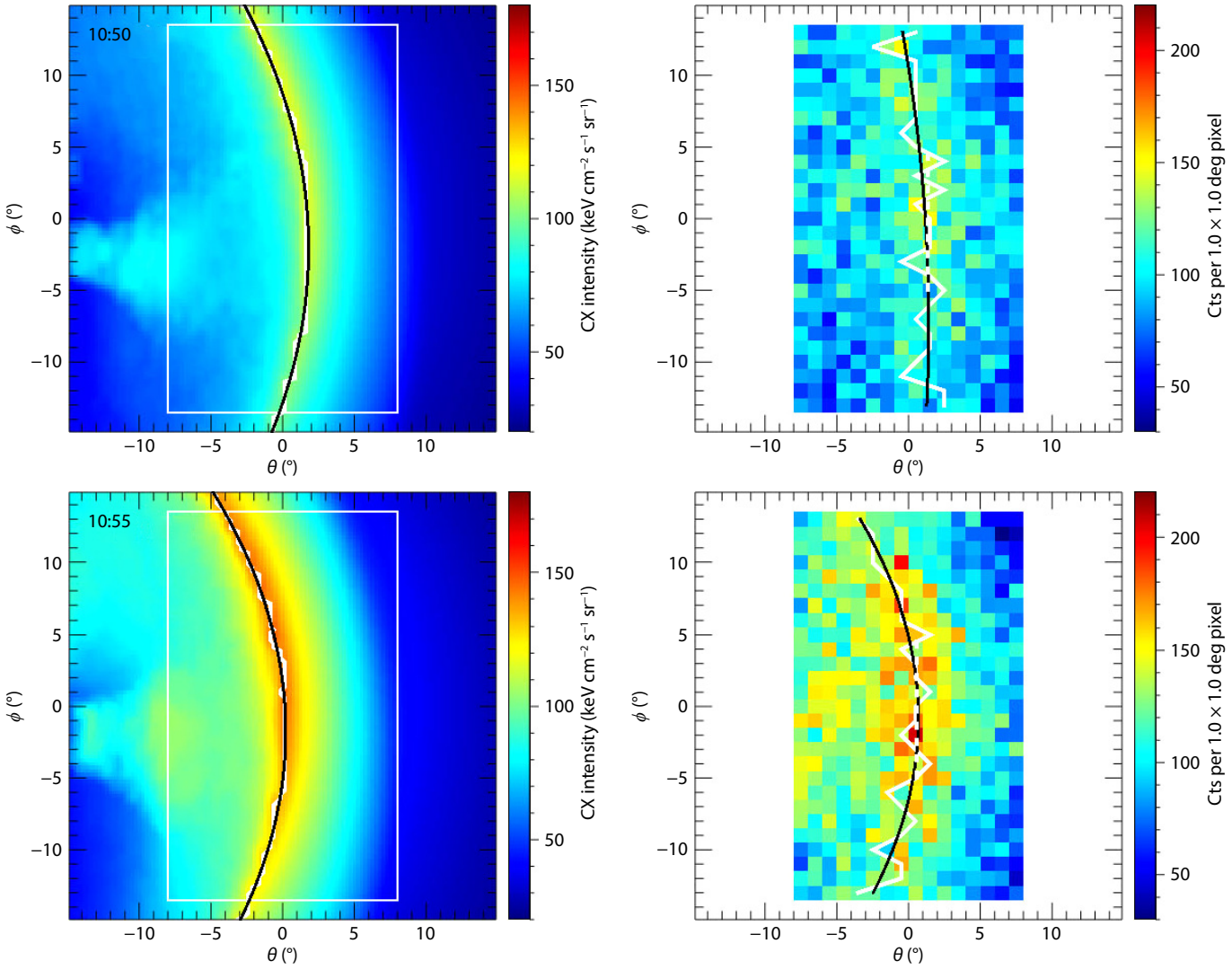

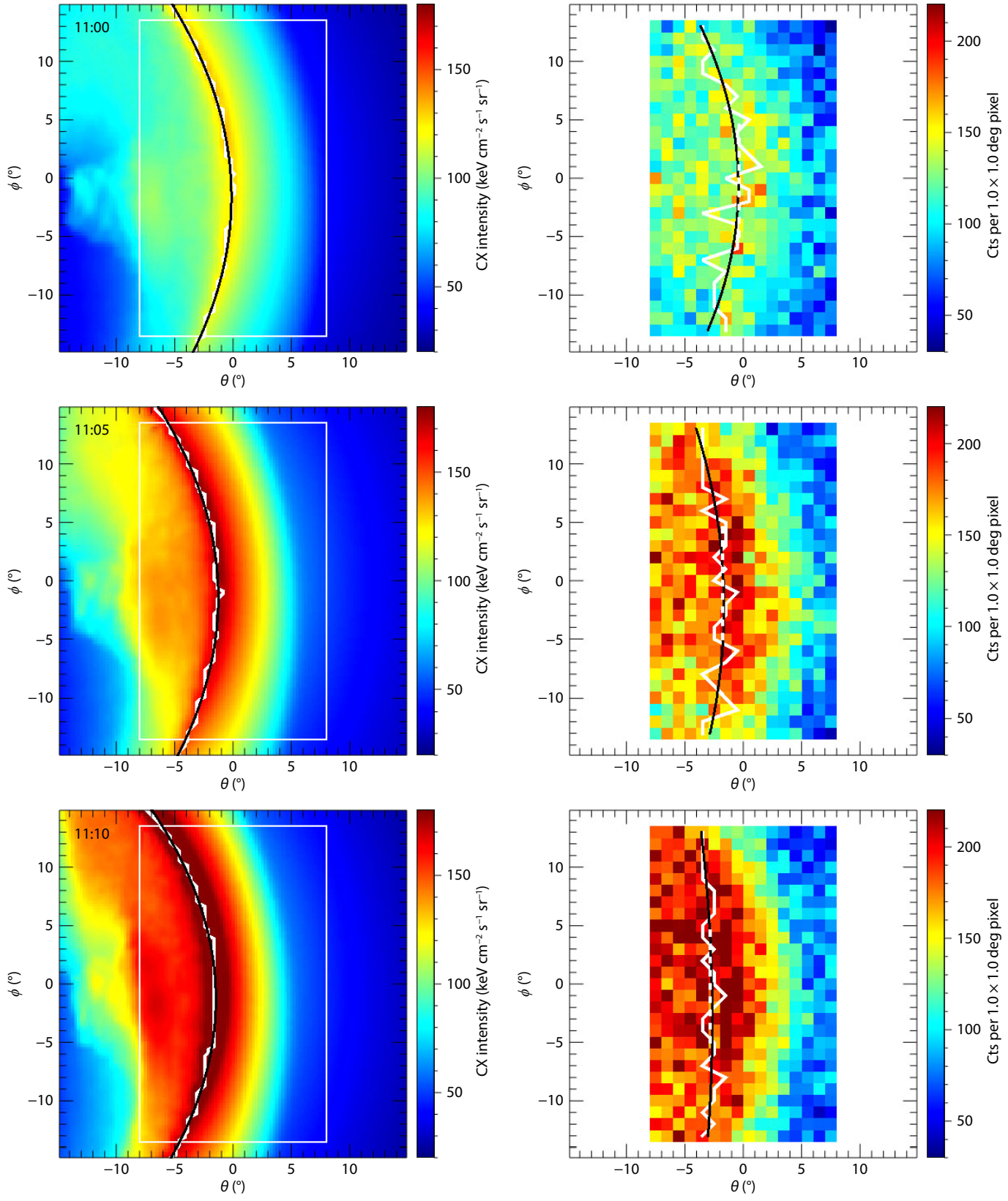

Figure 3. Integrated emissivity along the line-of-sight (left) and Soft X-ray Imager (SXI) count maps (right) between 10:50 and 11:10 UT. The white and black lines indicate the location of I_X and SXI count maxima (see details in text).The horizontal axis indicates angles along the Sun–Earth line, where one degree corresponds to ~0.3 R_E.

The arc of strong I_X (left panels) passing through the central part of the plots matches the magnetosheath region near the subsolar magnetopause. The bright spot closer to the Earth than the arc corresponds to the cusps. The arc moves earthward, whereas the bright spot moves sunward with time (from 10:50 to 11:10 UT). The arc motion is explained by the earthward magnetopause motion, whereas the bright spot motion may be explained by the cusp motion toward low latitudes, as expected for a southward IMF (e.g., Akasofu et al., 1973; Carbary and Meng, 1986). Accordingly, the I_X maximum increases with time, from 120 keV cm^{-2} s^{-1} sr^{-1} at 10:50 UT to 200 keV cm^{-2} s^{-1} sr^{-1} at 11:10 UT, because the emissivity is higher when the magnetopause is closer to the Earth. The SXI count maps (right panels in Figure 3) obtained with the integration time of 300 seconds are noisy, but we can clearly see the locations of count maxima in the arcs. These locations are highlighted by white and black lines obtained by finding averages and using polynomial interpolation, as explained below.

We find the running averages over five pixels along the horizontal axis (the size of the pixel on count maps is 1° × 1°). For each horizontal slice, we find the maximum of counts and show their positions by the white line. The black lines display second-degree polynomial fits for the white lines. We apply the same method for I_X on the left panels and count maps on the right panels. Because the locations of I_X maxima can be determined very accurately, we consider the black lines on the left panels as the references. The difference between the left and right black lines is relatively small near the subsolar point (i.e., near $\phi = 0$), but it increases toward the flanks. The intersections of black lines with $\phi = 0$ are then used to find the magnetopause standoff distance. Samsonov et al. (2022b) have presented more examples of using this method, along with some discussion.

3.3 Standoff Distance Calculated from Count Maps

We use the assumption that the maximum integrated emissivity occurs on lines-of-sight in the direction tangent to the magnetopause surface, and we interpolate the magnetopause by using the formula of Shue JH et al. (1997). Contrary to the assumptions by Jorgensen et al. (2019a) and Sun TR et al. (2020), we use the original axisymmetrical magnetopause as suggested by Shue JH et al. (1997). We show below that this assumption does not result in a large error because the tangent lines touch the magnetopause close to the subsolar point. Furthermore, we calculate the flaring parameter α by using the solar wind dynamic pressure and B_z according to Shue JH et al. (1998). Thus the magnetopause is defined as follows:

$$r = R_{SUB}\left(\frac{2}{1+\cos\theta}\right)^{\alpha} \text{ and } \alpha = [0.58 - 0.007B_z][1 + 0.024\ln(P_d)].$$

Here, R_{SUB} is the standoff distance, θ is the angle between the Sun–Earth line and r, and B_z and P_d are the IMF B_z and solar wind dynamic pressure. We use the solar wind conditions only for calculating α and find R_{SUB} for a known r, where r is the position of the tangent point. We can roughly estimate R_{SUB} by using the MHD solutions (see below), making a set of R_{SUB} around this MHD estimate, and choosing the one from them for which the direction of maximum integrated emissivity better matches the location of the tangent point at the magnetopause.

The spacecraft location at (6.57, −5.94, 17.33) R_E is almost strictly above the aim point at (7.0, 0.0, 0.0) R_E; therefore, we make the same analysis for another spacecraft location closer to the terminator plane (i.e., plane $x = 0$) at (2.34, −2.30, 16.34) R_E and compare the results of the calculated standoff distance. Both the first and second spacecraft locations are along the planned SMILE trajectory. We find the tangent points and then the magnetopause standoff distance by using the assumed magnetopause shape. Figure 4 displays the standoff distance calculated by the different methods: the open–closed boundary (solid black line) and the maximum density gradient (dashed black line) obtained directly from the MHD simulations, and the standoff distance calculated from the maximum integrated emissivity (pluses) and from the maximum SXI counts (squares) for the two spacecraft positions (blue and red). The maximum density gradient appears because the density in the magnetosheath is usually 1 to 2 orders higher than the density in the dayside magnetosphere. This results in a large density gradient located nearly at the magnetopause position. Indeed, the difference between the R_{SUB} obtained for the open–closed boundary and the maximum density gradient is relatively small, so we can define the "true" magnetopause as the maximum density gradient (also taking into account that X-ray emissivity is supposed to be proportional to the density). We calculate the standard deviations from the expected R_{SUB} for all estimates below.

Table 1 quantifies the results in Figure 4. The immediate magnetopause response to the ST occurs between 10:50 and 11:10 UT. During these 20 minutes, the R_{SUB} obtained from the maximum density gradient changes from 7.43 to 6.38 R_E (i.e., moves 1.05 R_E earthward). The R_{SUB} calculated from the open–closed boundary moves 1.03 R_E earthward (i.e., almost the same distance). The first row in Table 1 displays the corresponding differences in R_{SUB} between 10:50 and 11:10 UT calculated from the integrated emissivity and count maps. Only the difference in the last column (counts for position 2) differs distinctly from the expected one.

Table 1. Difference in R_{SUB} at 10:50 and 11:10 UT, the standard deviations (or the root mean square deviations), and the maximal absolute errors in the interval from 10:50 to 11:15 UT calculated from the integrated emissivity (I_X) plots and from the Soft X-ray Imager count maps for spacecraft positions 1 and 2.

	Max(I_x) position 1	Max(I_x) position 2	Max(counts) position 1	Max(counts) position 2
R_{SUB}(10:50)−R_{SUB}(11:10), R_E	1.00	1.02	1.23	1.42
σ, R_E	0.09	0.11	0.17	0.16
Max(|ΔR_{SUB}|), R_E	0.16	0.20	0.24	0.24

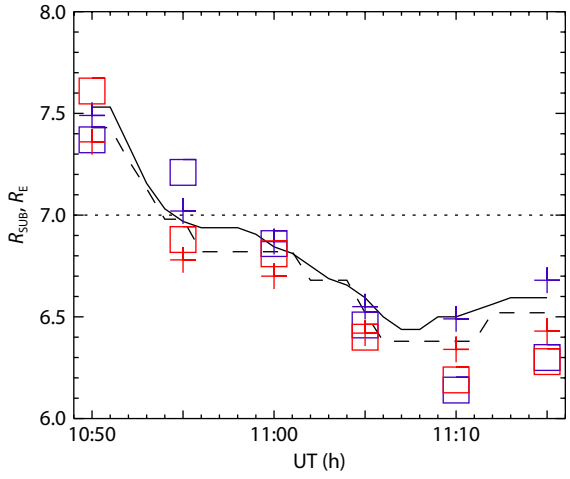

Figure 4. Magnetopause standoff distance during southward IMF turning: the boundary between open and close field lines (solid black line), the maximum of the density gradient (dashed black line), results obtained from the integrated emissivity (pluses), results obtained from the Soft X-ray Imager count maps (squares). The violet and red colors (for pluses and squares) correspond to spacecraft positions 1 and 2 (see details in text).

The second row exhibits the root mean square deviations with respect to the maximum density gradient R_{SUB}. Here, we consider the six points between 10:50 and 11:15 UT shown in Figure 4. The deviations are slightly higher for the count maps than for the integrated emissivity plots because the count maps contain noise, although the errors are still less than 0.2 R_E. The bottom row shows the maximal absolute differences for the same six points, and they do not exceed 0.24 R_E. Overall, this result demonstrates that we can find the changes in the standoff distance in response to the ST with high accuracy for both spacecraft positions even when using the simple image processing methods and the assumption about the axisymmetric magnetopause shape.

4. Conclusions

In this study, we demonstrate how the SXI instrument on board the SMILE mission can be used to observe magnetopause motion in response to an ST. We consider a directional IMF discontinuity with a large IMF B_z change but with a nearly constant solar wind density and V_x. We simulate this event by using the SWMF MHD model and calculate the X-ray emissivity and SXI count maps. The magnetosphere is moderately compressed at the time of the ST impact, with a magnetopause standoff distance varying around 7.0 R_E. Respectively, we can visually observe the region of maximum counts on the maps with a 5-minute integration time and watch this region move earthward as a result of the earthward magnetopause motion. Using averaging and a polynomial fit, we find the locations of the maximum counts at the subsolar point. Then assuming the axisymmetric magnetopause shape defined by the formula of Shue JH et al. (1997), we find the magnetopause standoff distance from the integrated emissivity and SXI count maps. We compare these estimates of the standoff distance with those obtained from the MHD simulations. We consider two spacecraft positions close to apogee: the one is nearly above the subsolar point, and the other is near the terminator plane.

We conclude that the estimated standoff distance during the ST event agrees well with the MHD results. If we consider the standoff distance obtained by the maximum density gradient in the MHD solution as the expected standoff distance, the standard deviations for the standoff distance obtained from count maps do not exceed 0.2 R_E in the 25-minute time interval around the ST. Moreover, the maximal absolute difference is 0.24 R_E, which is two times smaller than the science requirement for the SXI instrument of 0.5 R_E. The forthcoming SMILE observations will validate the MHD simulations and reveal whether the state-of-the-art MHD models can reproduce the reconnection process well at the dayside magnetopause.

Acknowledgments

This work was carried out using the SWMF/BATSRUS tools developed at the University of Michigan Center for Space Environment Modeling available through the NASA Community Coordinated Modeling Center (http://ccmc.gsfc.nasa.gov). In particular, we used results of the runs Andrey_Samsonov_071522_2. AAS and GBR acknowledge support from the UK Space Agency under Grant Number ST/T002964/1. Research by AAS was partly supported by the International Space Science Institute (ISSI) in Bern, through ISSI International Team Project Number 523 ("Imaging the Invisible: Unveiling the Global Structure of Earth's Dynamic Magnetosphere").

References

Akasofu, S. I., Perreault, P. D.,Yasuhara, F., and Meng, C. I. (1973). Auroral substorms and the interplanetary magnetic field. *J. Geophys. Res.*, *78*(31), 7490–7508. https://doi.org/10.1029/JA078i031p07490

Aubry, M. P., Russell, C. T., and Kivelson, M. G. (1970). Inward motion of the magnetopause before a substorm. *J. Geophys. Res.*, *75*(34), 7018–7031. https://doi.org/10.1029/JA075i034p07018

Branduardi-Raymont, G., Wang, C., Escoubet, C. P., Adamovic, M., Agnolon, D., Berthomier, M., Carter, J. A., Chen, W., Colangeli, L., …Zhu, Z. (2018). SMILE definition study report (No. 1). European Space Agency, ESA/SCI.

Carbary, J. F., and Meng, C. I. (1986). Correlation of cusp latitude with B_z and *AE* (12) using nearly one year's data. *J. Geophys. Res.*: *Space Phys.*., *91*(A9), 10047–10054. https://doi.org/10.1029/JA091iA09p10047

Carter, J. A., Sembay, S., and Read, A. M. (2010). A high charge state coronal mass ejection seen through solar wind charge exchange emission as detected by *XMM–Newton*. *Mon. Not. Roy. Astronom. Soc.*, *402*(2), 867–878. https://doi.org/10.1111/j.1365-2966.2009.15985.x

Collier, M. R., and Connor, H. K. (2018). Magnetopause surface reconstruction from tangent vector observations. *J. Geophys. Res.*: *Space Phys.*, *123*(12), 10189–10199. https://doi.org/10.1029/2018JA025763

Connor, H. K., Sibeck, D. G., Collier, M. R., Baliukin, I. I., Branduardi-Raymont, G., Brandt, P. C., Buzulukova, N. Y., Collado-Vega, Y. M., Escoubet, C. P., … Zoennchen, J. H. (2021). Soft X-ray and ENA imaging of the Earth's dayside magnetosphere. *J. Geophys. Res.*: *Space Phys.*, *126*(3), e2020JA028816. https://doi.org/10.1029/2020JA028816

Cravens, T. E., Robertson, I. P., and Snowden, S. L. (2001). Temporal variations of geocoronal and heliospheric X-ray emission associated with the solar wind interaction with neutrals. *J. Geophys. Res.*: *Space Phys.*, *106*(A11), 24883–24892. https://doi.org/10.1029/2000JA000461

Guo, Y. H., Sun, T. R., Wang, C., and Sembay, S. (2022). Deriving the magnetopause position from wide field-of-view Soft X-ray Imager simulation. *Sci. China Earth Sci.*, *65*(8), 1601–1611. https://doi.org/10.1007/s11430-021-9937-y

Jorgensen, A. M., Sun, T. R., Wang, C., Dai, L., Sembay, S., Wei, F., Guo, Y. H., and Xu, R. L. (2019a). Boundary detection in three dimensions with application

to the SMILE mission: the effect of photon noise. *J. Geophys. Res.*: *Space Phys.*, *124*(6), 4365–4383. https://doi.org/10.1029/2018JA025919

Jorgensen, A. M., Sun, T. R., Wang, C., Dai, L., Sembay, S., Zheng, J. H., and Yu, X. Z. (2019b). Boundary detection in three dimensions with application to the SMILE mission: the effect of model-fitting noise. *J. Geophys. Res.*: *Space Phys.*, *124*(6), 4341–4355. https://doi.org/10.1029/2018JA026124

Jorgensen, A. M., Xu, R., Sun, T., Huang, Y., Li, L., Dai, L., and Wang, C. (2022). A theoretical study of the tomographic reconstruction of magnetosheath X-ray emissions. *J. Geophys. Res.*: *Space Phys.*, *127*(4), e2021JA029948. https://doi.org/10.1029/2021JA029948

Kuntz, K. D., Collado-Vega, Y. M., Collier, M. R., Connor, H. K., Cravens, T. E., Koutroumpa, D., Porter, F. S., Robertson, I. P., Sibeck, D. G., … Walsh, B. M. (2015). The solar wind charge exchange production factor for hydrogen. *Astrophys. J.*, *808*(2), 143. https://doi.org/10.1088/0004-637X/808/2/143

Maltsev, Y. P., and Lyatsky, W. B. (1975). Field-aligned currents and erosion of the dayside magnetosphere. *Planet. Space Sci.*, *23*(9), 1257–1260. https://doi.org/10.1016/0032-0633(75)90149-x

Powell, K. G., Roe, P. L., Linde, T. J., Gombosi, T. I., and De Zeeuw, D. L. (1999). A solution-adaptive upwind scheme for ideal magnetohydrodynamics. *J. Comput. Phys.*, *154*(2), 284–309. https://doi.org/10.1006/jcph.1999.6299

Read, A. (2024). On the Apparent Line-of-Sight Alignment of the Peak X-ray Intensity of the Magnetosheath and the Tangent to the Magnetopause, as Viewed by SMILE-SXI. This issue.

Robertson, I. P., and Cravens, T. E. (2003). X-ray emission from the terrestrial magnetosheath. *Geophys. Res. Lett.*, *30*(8), 1439. https://doi.org/10.1029/2002GL016740

Samsonov, A., Carter, J. A., Read, A., Sembay, S., Branduardi-Raymont, G., Sibeck, D., and Escoubet, P. (2022a). Finding magnetopause standoff distance using a Soft X-ray Imager: 1. Magnetospheric masking. *J. Geophys. Res.*: *Space Phys.*, *127*(12), e2022JA030848. https://doi.org/10.1029/2022JA030848

Samsonov, A., Sembay, S., Read, A., Carter, J. A., Branduardi-Raymont, G., Sibeck, D., and Escoubet, P. (2022b). Finding magnetopause standoff distance using a Soft X-ray Imager: 2. Methods to analyze 2-D X-ray images. *J. Geophys. Res.*: *Space Phys.*, *127*(12), e2022JA030850. https://doi.org/10.1029/2022JA030850

Sembay, S., Alme, A. L., Agnolon, D., Arnold, T., Beardmore, A., Belén Balado Margeli, A., Bicknell, C., Bouldin, C., Branduardi-Raymont, G., …Yang, S. (2024). The Soft X-ray Imager (SXI) on the SMILE Mission. This issue.

Shue, J. H., Chao, J. K., Fu, H. C., Russell, C. T., Song, P., Khurana, K. K., and Singer, H. J. (1997). A new functional form to study the solar wind control of the magnetopause size and shape. *J. Geophys. Res.*: *Space Phys.*, *102*(A5), 9497–9511. https://doi.org/10.1029/97JA00196

Shue, J. H., Song, P., Russell, C. T., Steinberg, J. T., Chao, J. K., Zastenker, G., Vaisberg, O. L., Kokubun, S., Singer, H. J., …Kawano, H. (1998). Magnetopause location under extreme solar wind conditions. *J. Geophys. Res.*: *Space Phys.*, *103*(A8), 17691–17700. https://doi.org/10.1029/98JA01103

Sibeck, D. G., Allen, R., Aryan, H., Bodewits, D., Brandt, P., Branduardi-Raymont, G., Brown, G., Carter, J. A., Collado-Vega, Y. M., …Wing, S. (2018). Imaging plasma density structures in the soft X-rays generated by solar wind charge exchange with neutrals. *Space Sci. Rev.*, *214*(4), 79. https://doi.org/10.1007/s11214-018-0504-7

Sun, T. R., Wang, C., Sembay, S. F., Lopez, R. E., Escoubet, C. P., Branduardi-Raymont, G., Zheng, J. H., Yu, X. Z., Guo, X. C., …Guo, Y. H. (2019). Soft x-ray imaging of the magnetosheath and cusps under different solar wind conditions: MHD simulations. *J. Geophys. Res.*: *Space Phys.*, *124*(4), 2435–2450. https://doi.org/10.1029/2018JA026093

Sun, T. R., Wang, C., Connor, H. K., Jorgensen, A. M., and Sembay, S. (2020). Deriving the magnetopause position from the soft X-ray image by using the tangent fitting approach. *J. Geophys. Res.*: *Space Phys.*, *125*(9), e2020JA028169. https://doi.org/10.1029/2020JA028169

Tóth, G., Sokolov, I. V., Gombosi, T. I., Chesney, D. R., Clauer, C. R., de Zeeuw, D. L., Hansen, K. C., Kane, K. J., Manchester, W. B., … Kóta, J. (2005). Space Weather Modeling Framework: a new tool for the space science community. *J. Geophys. Res.*: *Space Phys.*, *110*(A12), A12226. https://doi.org/10.1029/2005JA011126

Tóth, G., van der Holst, B., Sokolov, I. V., De Zeeuw, D. L., Gombosi, T. I., Fang, F., Manchester, W. B., Meng, X., Najib, D., …Opher, M. (2012). Adaptive numerical algorithms in space weather modeling. *J. Comput. Phys.*, *231*(3), 870–903. https://doi.org/10.1016/j.jcp.2011.02.006

Tsyganenko, N. A., and Sibeck, D. G. (1994). Concerning flux erosion from the dayside magnetosphere. *J. Geophys. Res.*: *Space Phys.*, *99*(A7), 13425–13436. https://doi.org/10.1029/94JA00719

Wang, C., and Sun, T. R. (2022). Methods to derive the magnetopause from soft X-ray images by the SMILE mission. *Geosci. Lett.*, *9*(1), 30. https://doi.org/10.1186/s40562-022-00240-z